Monthly Notices of the ROYAL ASTRONOMICAL SOCIETY

MNRAS **529,** L33–L40 (2024) https://doi.org/10.1093/mnrasl/slad195
Advance Access publication 2023 December 28

The metamorphosis of the Type Ib SN 2019yvr: late-time interaction

Lucía Ferrari [1,2★] Gastón Folatelli,[1,2,3] Hanindyo Kuncarayakti,[4,5] Maximilian Stritzinger,[6] Keiichi Maeda [7] Melina Bersten,[1,2,3] Lili M. Román Aguilar,[1,2] M. Manuela Sáez,[8,9] Luc Dessart,[10] Peter Lundqvist [11] Paolo Mazzali,[12,13] Takashi Nagao [4,14,15] Chris Ashall,[16] Subhash Bose [6,17] Seán J. Brennan,[11] Yongzhi Cai,[18,19,20] Rasmus Handberg [6] Simon Holmbo,[6] Emir Karamehmetoglu,[6] Andrea Pastorello,[21] Andrea Reguitti [21,22] Joseph Anderson,[23] Ting-Wan Chen,[24] Lluís Galbany,[25,26] Mariusz Gromadzki [27] Claudia P. Gutiérrez [25,26] Cosimo Inserra [28] Erkki Kankare,[4] Tomás E. Müller Bravo,[25,26] Seppo Mattila,[4,29] Matt Nicholl,[30] Giuliano Pignata,[31] Jesper Sollerman [11] Shubham Srivastav[32] and David R. Young[32]

Affiliations are listed at the end of the paper

Accepted 2023 December 12. Received 2023 December 7; in original form 2023 September 30

ABSTRACT

We present observational evidence of late-time interaction between the ejecta of the hydrogen-poor Type Ib supernova (SN) 2019yvr and hydrogen-rich circumstellar material (CSM), similar to the Type Ib SN 2014C. A narrow H α emission line appears simultaneously with a break in the light-curve decline rate at around 80–100 d after explosion. From the interaction delay and the ejecta velocity, under the assumption that the CSM is detached from the progenitor, we estimate the CSM inner radius to be located at $\sim$6.5–9.1 $\times$ 10^{15} cm. The H α emission line persists throughout the nebular phase at least up to +420 d post-explosion, with a full width at half maximum of $\sim$2000 km s^{-1}. Assuming a steady mass-loss, the estimated mass-loss rate from the luminosity of the H α line is $\sim$3–7 $\times$ 10^{-5} $M_\odot$ yr^{-1}. From hydrodynamical modelling and analysis of the nebular spectra, we find a progenitor He-core mass of 3–4 $M_\odot$, which would imply an initial mass of 13–15 $M_\odot$. Our result supports the case of a relatively low-mass progenitor possibly in a binary system as opposed to a higher mass single star undergoing a luminous blue variable phase.

Key words: supernovae: general – supernovae: individual: SN 2019yvr.

1 INTRODUCTION

Supernovae (SNe) are among the most powerful explosions in the Universe, and their study provides valuable insights into a multitude of astrophysical processes including stellar evolution, the subsequent formation of compact objects, and the chemical enrichment of the Universe. A substantial fraction of SNe are associated with the collapse of the iron cores of massive stars, called core-collapse SNe (CCSNe). CCSNe are classified based on their spectral characteristics. Objects with H features are classified as Type II, those lacking H but exhibiting He are of Type Ib, and those with no H nor He are of Type Ic (for a contemporary and concise review, see Stritzinger et al. 2023b, and references therein). Although relatively rare, the H-poor stripped-envelope SNe are of particular interest as they are most likely linked to the death of a He or C + O star, as an analogue of Wolf–Rayet stars, which experienced significant mass-loss either through strong stellar winds or interaction with a binary companion (e.g. Woosley, Langer & Weaver 1993; Podsiadlowski et al. 2004; Smith 2014). Moreover, it has been proposed that the progenitor envelope could be removed by a combination of both processes, i. e. hybrid mass-loss (Fang et al. 2019; Sun, Maund & Crowther 2023).

A small but growing number of Type Ib (e.g. Milisavljevic et al. 2015; Vinko et al. 2017; Mauerhan et al. 2018; Chandra et al. 2020) and Type Ic SNe (Kuncarayakti et al. 2018; Tartaglia et al. 2021; Stritzinger et al. 2023a) exhibit signatures of circumstellar interaction (CSI) in optical wavelengths. CSI occurs when rapidly expanding SN ejecta shock a dense circumstellar material (CSM), originated from the progenitor star itself, or from a companion star (e.g. Chevalier & Fransson 1994; Fransson et al. 2002; Yoon 2017). Signatures of CSI in some cases are revealed in the spectra as narrow Balmer emission lines, reminiscent to the hallmark feature of Type IIn SNe (e.g. Schlegel 1990; Taddia et al. 2013), as well as in some cases high-ionization coronal lines, and/or excesses of flux in different regions of the electromagnetic spectrum (e.g. Stritzinger et al. 2012).

In this paper, we examine SN 2019yvr, which was initially classified as a Type Ib SN (Dimitriadis 2019), but eventually developed SN IIn-like features. Based on pre-explosion *Hubble Space Telescope* archival images, Kilpatrick et al. (2021) found a point source at the location of SN 2019yvr. The spectral energy distribution (SED) of the source suggests a cool and luminous progenitor candidate, in contradiction with the He star picture of a SN Ib progenitor. They also discuss a binary scenario but also find it incompatible with a Type Ib SN progenitor. Sun et al. (2022) explored several scenarios by performing an environmental study, and proposed a

★ E-mail: luciaferrari4@gmail.com

binary system, composed of a hot and compact SN progenitor and a yellow hypergiant (YHG) companion. SN 2019yvr therefore provides an opportunity to understand better the pre-SN evolution of interacting events' progenitors.

The present work focuses on the appearance of the CSI features in SN 2019yvr, the late-time interaction, and particular progenitor properties such as the pre-SN mass and mass-loss rate. We will complement this analysis with an upcoming paper by Ferrari et al. (in preparation) where we will provide a detailed analysis of the full photometric and spectroscopic evolution.

2 OBSERVATIONS

SN 2019yvr was first reported by the Asteroid Terrestrial-impact Last Alert System on 2019 December 27.5 UT (Tonry et al. 2019), and classified two days later as a Type Ib SN (Dimitriadis et al. 2019; Muller et al. 2019). Based on the last non-detection from the Zwicky Transient Facility (Masci et al. 2019), we adopt an explosion epoch as JD = 2458839.89±3.84. The SN is located in the nearby Galaxy NGC 4666, which hosted the Type Ia SN ASASSN-14lp (Shappee et al. 2016). We adopt their derived distance of 14.7 ± 1.5 Mpc. See section 1 of the Supplementary Material for details on the discovery, the estimated explosion date and the adopted distance.

The data employed in this study are part of a larger set of multiband optical light curves and a series of spectra (Ferrari et al., in preparation). Here we present *BVgri*-band photometry measured from images obtained by the NUTS[1] (Nordic optical telescope Unbiased Transient Survey) and ASAS-SN[2] (All-Sky Automated Survey for Supernovae) collaborations using the 2.56-m NOT telescope equipped with ALFOSC (Andalucia Faint Object Spectrograph and Camera) and the 1-m Las Cumbres Observatory Global Telescope (LCOGT) network respectively. The NOT images were reduced using the PYRAF-based ALFOSCGUI[3] reduction pipeline developed by E. Cappellaro, while fully processed LCOGT images were downloaded from the observatory's data archive.

Host-galaxy subtraction was performed on all science frames using template images obtained prior to 2019. Point-spread-function photometry of SN 2019yvr was then measured relative to stars in the field using the Aarhus-Barcelona FLOWS project's automated pipeline.[4] The photometry is tabulated in section 2 of the Supplementary Material.

We also present eight low-resolution and one high-resolution optical spectra, which are summarized in the journal of spectroscopic observations (section 2 of the Supplementary Material). In summary, four spectra were obtained by ePESSTO + (Smartt et al. 2015) with the European Southern Observatory (ESO) 3.58-m New Technology Telescope (Buzzoni et al. 1984) equipped with the ESO Faint Object Spectrograph and Camera optical (EFOSC2), three by NUTS with the NOT (+ALFOSC), and one spectrum was obtained with the ESO 8.4-m Very Large Telescope FOcal Reducer and low-dispersion Spectrograph (Appenzeller et al. 1998), as part of the FORS + Survey of Supernovae in Late Times program (see Kuncarayakti et al. 2022). A high-resolution spectrum was obtained with the 8.2-m Subaru Telescope equipped with the High Dispersion Spectrograph (Noguchi et al. 2002). The spectroscopic observations were reduced following standard techniques using the respective instrument pipelines.

[1] http://nuts.sn.ie/.
[2] https://www.astronomy.ohio-state.edu/asassn/.
[3] http://graspa.oapd.inaf.it/foscgui.html.
[4] https://github.com/SNflows.

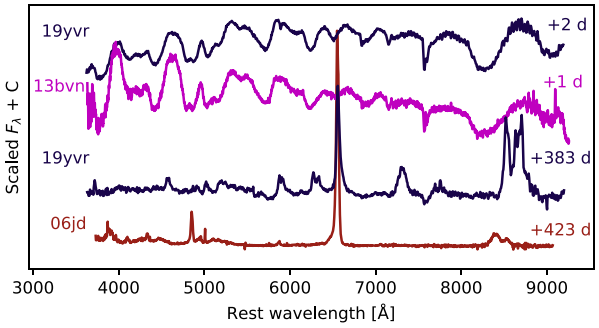

Figure 1. SN 2019yvr transitions from a SN Ib spectrum around maximum to a Type IIn-like spectrum at late phase. Comparison data include a similar phase spectrum of the SN Ib iPTF13bvn (Srivastav, Anupama & Sahu 2014) and the Type IIn SN 2006jd (Stritzinger et al. 2012). Spectra are corrected by redshift and not corrected by extinction.

The Milky Way reddening along the line of sight is $E(B-V)_{\rm MW} = 0.022$ mag (i.e. $A_{\rm V}^{\rm MW} = 0.068$ mag, Schlafly & Finkbeiner 2011, assuming $R_{\rm V} = 3.1$). After comparing the observed colour curves of SN 2019yvr with the intrinsic colour-curve templates from Stritzinger et al. (2018), analysing the diffuse interstellar band at 5780 Å and the Na I D lines in the high-resolution spectrum from the Subaru telescope, we adopt a host-galaxy reddening of $E(B-V)_{\rm host} = 0.57 \pm 0.09$ mag. This value is in agreement with the estimate of Kilpatrick et al. (2021) of $0.51^{+0.27}_{-0.16}$ mag and with that published in Rodríguez, Maoz & Nakar (2022) of 0.56 ± 0.09 mag. Details on the reddening estimation are presented in section 3 of the Supplementary Material.

3 SIGNATURES OF CSM INTERACTION

3.1 Emergence of H α emission

SN 2019yvr showed H α emission at late times similarly to SN 2014C, which in that case was interpreted as a result of interaction between the ejecta and H-rich CSM (e.g. Milisavljevic et al. 2015; Margutti et al. 2017). In Fig. 1, we compare the spectra of SN 2019yvr obtained +2 d and +383 d past the epoch of *B*-band maximum, JD = 2458851.6 (see table 1 of the Supplementary Material). Throughout the paper we will refer the phases to this date unless otherwise specified. While the first spectrum is consistent with that of typical SNe Ib, the late-phase spectrum clearly exhibits the transformation to a SN IIn-like spectrum.

The temporal coverage of SN 2019yvr observations allows us to study the moment when signatures of interaction become apparent. This is depicted in Fig. 2 where we show the evolution of the spectra around the He I λ6678 (which includes H α) and the He I λ7065 lines between +42 d and +118 d. The +118 d spectrum clearly exhibits H α in emission, whereas the previous spectra show an absorption at the same wavelength. While the absorption due to He I λ6678 becomes substantially weaker with time before the H α emission emerges, the absorption due to He I λ7065 remains roughly constant.

This phenomenon can be appreciated in the evolution of the absorption pseudo-equivalent width (pEW)[5] of both lines. We measured pEW using the *splot* task from IRAF five times to account for values

[5] The term 'pseudo-equivalent width' is used because the actual continuum flux is unknown and we therefore fit a 'pseudo-continuum' between the local maxima at both sides of the line.

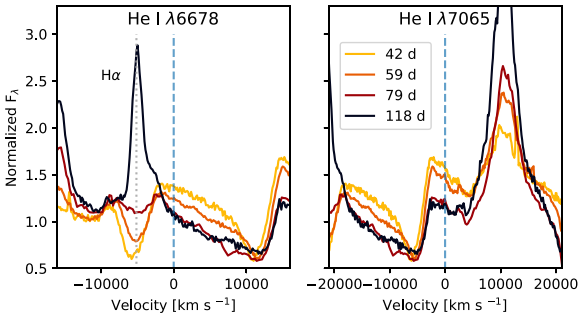

Figure 2. Evolution of the He I λ6678 and He I λ7065 features of SN 2019yvr from +42 d to +118 d plotted in velocity space. Dashed vertical lines indicate the 0 km s^{-1} position, while in the left panel the dotted vertical line indicates the rest wavelength of H α. Complete spectra are displayed in section 4 of the Supplementary Material.

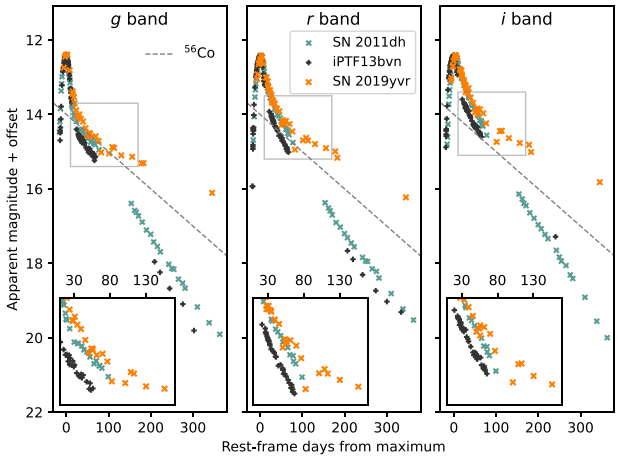

Figure 3. Light curves of SN 2019yvr compared with those of SN 2011dh (Ergon et al. 2015) and iPTF13bvn (Fremling et al. 2016), shifted in magnitudes to coincide at the peak. Dashed lines correspond to ^{56}Co decay. The post-maximum light curves of SN 2019yvr begin to deviate from the normal decay line of the comparison objects beginning around +80 d.

with their corresponding errors. For He I λ6678, we obtain pEW = 40.4 ± 0.9, 26.9 ± 0.6, and 10.4 ± 0.3 Å at 42, 59, and 79 d, respectively, whereas for He I λ7065 the values are nearly constant or even rising (91 ± 1.4, 106 ± 1.4, and 118 ± 2.2 Å). The same behaviour as that of He I λ7065 is seen in He I λ5876 but we note that the Na I D doublet may contaminate the latter line and thus it is not shown here. We interpret the weakening of the He I λ6678 absorptions as a result of the appearance of H α in emission at a similar wavelength.

Assuming a detached CSM from the progenitor, we conclude that the strong ejecta–CSM interaction initiated sometime prior to +79 d.

3.2 Flattening in the light curves

The *gri*-band light curves are plotted in Fig. 3, compared with the Type IIb SN 2011dh and the Type Ib iPTF13bvn. The light curves of SN 2019yvr present a characteristic break in the post-maximum decline rate, leading to a flattening after +90 d. In Fig. 3, the break is evident in all optical bands by comparison with SNe that show a similar evolution around maximum light. Moreover, iPTF13bvn provided a very good match to the spectroscopic evolution of SN 2019yvr around maximum light. Although the spectral match to the SN IIb 2011dh is worse, its light curves provide a good match to our object around maximum light and are more complete than those of iPTF13bvn.

We interpret the sudden change in the slope of the light curves of SN 2019yvr as a result of an extra power source caused by sustained interaction between the SN ejecta and the CSM. This interpretation is supported by the nearly simultaneous appearance of H α emission in the spectra (see Section 3.1). From close inspection of Fig. 3, we conclude that the flattening in the light curves occurs in all bands between +70 and +90 d with respect to maximum light. This is in accordance with what was found in Section 3.1.

3.3 Properties of the CSM

Based on the light curves and spectral evolution, we have determined that the interaction power starts dominating the decay power between +70 d to +90 d (i.e. 75–105 d post our inferred explosion epoch). If we assume the presence of a detached CSM structure, the interaction delay indicates a distance to its inner boundary. By adopting a maximum ejecta velocity of ∼10 000 km s^{-1} from the bluest extent of the He I λλ6678, 7065 absorption components, this gives a distance of 6.5–9.1 × 10^{15} cm or 0.9–1.3 × 10^{5} R$_\odot$. These values are comparable to those obtained for SN 2001em (a SN Ic that showed late phase H α in emission, Chugai & Chevalier 2006); and SN 2014C (Milisavljevic et al. 2015). If the CSM was expelled by stellar winds with a velocity in the range of 50–100 km s^{-1}, the mass-loss must have occurred up until ∼20–60 yr prior to the explosion (assuming a detached CSM).

We further study the properties of the CSM by analysing the H α emission in the nebular phase. We measure the H α luminosity, $L_{\mathrm{H}\alpha}$, to derive the mass-loss rate from (e.g. Kuncarayakti et al. 2018)

$$\dot{M} = 2\,\frac{L_{\mathrm{H}\alpha}}{\epsilon_{\mathrm{H}\alpha}}\,\frac{v_{\mathrm{wind}}}{v_{\mathrm{shock}}^3},$$

where v_{wind} is the wind velocity at which the material was expelled during the final stages of the star's evolution, v_{shock} is the velocity of the colliding material, and $\epsilon_{\mathrm{H}\alpha}$ is an efficiency factor that we assume to be 0.01 (Chevalier & Fransson 1994).

We scaled our +383 d and +386 d spectra so that they matched the *r*-band photometry. They were corrected for extinction and the H α fluxes were then measured with *splot* in IRAF. We discard the measurement from the +426 d spectrum because it likely suffers from host-galaxy contamination. The resulting fluxes were 7.77 ± 0.19 × 10^{-14} erg s^{-1} cm^{-2} from the +383 d spectrum, and 8.44 ± 0.44 × 10^{-14} erg s^{-1} cm^{-2} from the +386 d spectrum, whose average yields a flux of 8.10 ± 0.47 × 10^{-14} erg s^{-1} cm^{-2}. With the distance given in Section 2, we obtained an H$_\alpha$ luminosity of L_α = 2.1 ± 0.6 × 10^{39} erg s^{-1}. For the shock velocity, we adopted 10 000 km s^{-1} based on typical values for SNe Ib (Liu et al. 2016). Assuming a wind velocity of v_{wind} = 50–100 km s^{-1}, the derived mass-loss rate range is ∼3 − 7 × 10^{-5} M$_\odot$ yr^{-1}. This is comparable to that of SN 2013df, which also shows a late-phase light curve flattening (Maeda et al. 2015). If a shock velocity of 2000 km s^{-1} is considered, this translates to an upper limit for the mass-loss rate of ∼4 − 8 × 10^{-3} M$_\odot$ yr^{-1}. A high density of the CSM may prevent the appearance of [O III] lines, but would not be enough to produce electron scattering wings in H α (see Section 4). The material could be distributed in a clumpy shell with cloud shocks of about 2000 km s^{-1} and faster, lower density shocks in between, which would be responsible for the H α wings.

4 NEBULAR SPECTRA

Nebular spectra of SN 2019yvr obtained on +383 d, +386 d, and +426 d are plotted in Fig. 4, along with a +371 d spectrum of SN 2014C and a +290 d spectrum of iPTF13bvn. These objects were classified as H-poor SNe Ib based on their early spectroscopy.[6] Similar to SN 2014C, SN 2019yvr developed a narrow ∼2000 km s^{-1} Hα emission at late times, although their profiles differ. While in SN 2019yvr the line is asymmetric and blue shifted by ∼300 km s^{-1}, SN 2014C showed a compound profile, with one broad ∼1200 km s^{-1} component overlapped with narrow ∼250 km s^{-1} Hα and [N II] λλ6548, 6583 components (Milisavljevic et al. 2015). The narrow components may be linked to CSM material undergoing photoionization caused by X-rays emitted by the interaction, though these could also result from contamination by an underlying H II region. The broad component is associated with the shock or ejected material colliding with the CSM. In the right panel of Fig. 4, we rebinned the spectrum of SN 2014C to match the resolution of the FORS spectrum of SN 2019yvr. We conclude that those narrow lines, if present, are not resolved by our observations. Another difference can be appreciated in the narrow emissions associated with Hβ and [O III] λλ4959, 5007 that are absent in the case of SN 2019yvr.

A striking feature is the strong Ca II near-infrared triplet, which is usually weaker than [O I] λλ6300, 6364 and [Ca II] λλ7291, 7324 in SESNe (Jerkstrand et al. 2015; Dessart et al. 2021, 2023a). This feature is detected in the +282 d spectrum of SN 2014C, but with a substantially weaker intensity (Milisavljevic et al. 2015) compared to SN 2019yvr.

Typical nebular emission lines are present, such as the aforementioned [O I], [Ca II], also Na I D, and [Mg I] λ4571. The oxygen doublet shows a double-peaked profile, with a ∼1300 km s^{-1} blueshift and a full width at half-maximum of ∼2000 and ∼2500 km s^{-1} for the bluer and redder component respectively, different from the one-component profile in SN 2014C. The Na I D emission presents a broad profile, with ISM absorption on top. The [Ca II] and [Mg I] lines show a single component profile. Line identifications are shown in Fig. 4.

The Hα profile provides insights into the geometry responsible for such emission. If the CSM was distributed in a spherical structure surrounding the SN, the profile should be box-shaped as in SN 1993J (Filippenko, Matheson & Barth 1994; Patat, Chugai & Mazzali 1995; Matheson et al. 2000) and SN 2013df (Maeda et al. 2015). The absence of such a profile suggests that the emission may not come from the outer layers of the ejecta interacting with the CSM, as the velocity should be higher (∼10000 km s^{-1}; see e.g. Dessart et al. 2023b). The ∼2000 km s^{-1} width the of Hα line indicates that the slower, inner part of the ejecta are interacting with a nearby, dense CSM. This CSM may take the form of a circumstellar disc which could be produced in a binary system, although detailed modelling is required to ascertain this possibility. It has been proposed for SN 2014C that the Hα emission comes from the interaction between the ejecta and a CSM with a torus-like structure (Thomas et al. 2022), which could be also the case for SN 2019yvr.

5 PROGENITOR PROPERTIES

In this section, we aim to constrain the progenitor mass, and then link it with what was obtained in Section 3. For this purpose, we consider three methods: (i) the early bolometric light curve modelling, (ii) the comparison of nebular spectra with synthetic nebular spectra from Dessart et al. (2023a), and (iii) the oxygen mass estimation from the [O I] λλ6300, 6364 flux following the procedure of Jerkstrand et al. (2014). Our results are summarized in Fig. 5.

5.1 Hydrodynamical model

We used the 1D Lagrangian hydrodynamic code (Bersten, Benvenuto & Hamuy 2011) to model the bolometric light curve and the photospheric velocity evolution of SN 2019yvr. As initial configurations for our hydrodynamical models, we adopted He stars of different masses from Nomoto & Hashimoto 1988, which follow the complete evolution of the stars with Zero Age Main Sequence (ZAMS) masses of 13, 15, 18, and 25 M$_\odot$, to the pre-SN conditions. The simulations' free parameters are the explosion energy (E), the ejected mass ($M_{\rm ej}$), the mass of synthesized ^{56}Ni ($M_{\rm Ni}$), and the extent of outward mixing of ^{56}Ni (as a fraction of the pre-SN mass). The energy is deposited at a certain mass coordinate, $M_{\rm cut}$, within the pre-SN structure. It is assumed that the matter inside $M_{\rm cut}$ collapses into a compact remnant while the outer mass is ejected.

We computed the bolometric light curve for SN 2019yvr based on (g–r) and (r–i) colour curves using the bolometric-correction versus colour calibrations for SNe Ib given by Lyman, Bersier & James (2014; see their table 2). We applied extinction and distance values as given in Section 2 to derive bolometric luminosities, and then averaged the results obtained from both colour indices. Finally, to approximate photospheric velocities, we measured the Fe II λ5169 line velocity from the location of the absorption minimum.

Fig. 5, panels (a) and (b), show the results of the modelling. Our preferred model corresponds to a pre-SN model with a mass of 3.3 M$_\odot$, $E = 4 \times 10^{50}$ erg, $M_{\rm Ni} = 0.088$ M$_\odot$ and an extensive mixing of 0.93. We also assume a $M_{\rm cut} = 1.5$ M$_\odot$, leading to an $M_{\rm ej} = 1.8$ M$_\odot$. However a model with a pre-SN mass of 4 M$_\odot$ also produces a reasonable match to the data. Therefore we propose progenitors with a pre-SN mass between 3 and 4 M$_\odot$, which corresponds to a ZAMS mass of 13–15 M$_\odot$.

We have also tested models with higher masses which require higher energy in order to reproduce the expansion velocities, leading to worse fitting to the light curve [see Fig. 5, panels (a) and (b)]. For these more massive progenitors, we found that no set of parameters can fit both the bolometric light curve and the velocities together. Specifically, in Fig. 5 we show two models corresponding to 8.0 M$_\odot$ pre-SN models with $E = 1$ foe and $E = 5$ foe, and equal values for $M_{\rm ej} = 6.2$ M$_\odot$ ($M_{\rm cut} = 1.8$ M$_\odot$), $M_{\rm Ni} = 0.1$ M$_\odot$, and mixing $= 0.98$. The first case reproduces well the velocities but not the bolometric light curve, and vice versa.

Since the lowest pre-SN mass model provided by Nomoto & Hashimoto (1988) is that of 3.3 M$_\odot$, we are not able to model the bolometric light curve and photospheric velocities for lower masses and constraint the inferior limit of the progenitor star mass with this approach. The derived ZAMS mass between 13 and 15 M$_\odot$ thus corresponds to an upper limit.

5.2 Model nebular spectra and the [O I]/[Ca II] ratio

The flux ratio of nebular [O I] λλ6300, 6364 to [Ca II] λλ7291, 7324 lines has been suggested as an indicator of the pre-SN mass (e.g. Fransson & Chevalier 1989; Maeda et al. 2007; Fang et al. 2022). We calculated these ratios on the +383 and the +426 d EFOSC2 spectra by fitting Gaussian profiles and subtracting the strong local continuum. In the case of [O I], we used two Gaussians to account

[6]Note that some authors suggested the possible presence of H features in the spectra of iPTF13bvn and SN 2014C (Kuncarayakti et al. 2015; Milisavljevic et al. 2015).

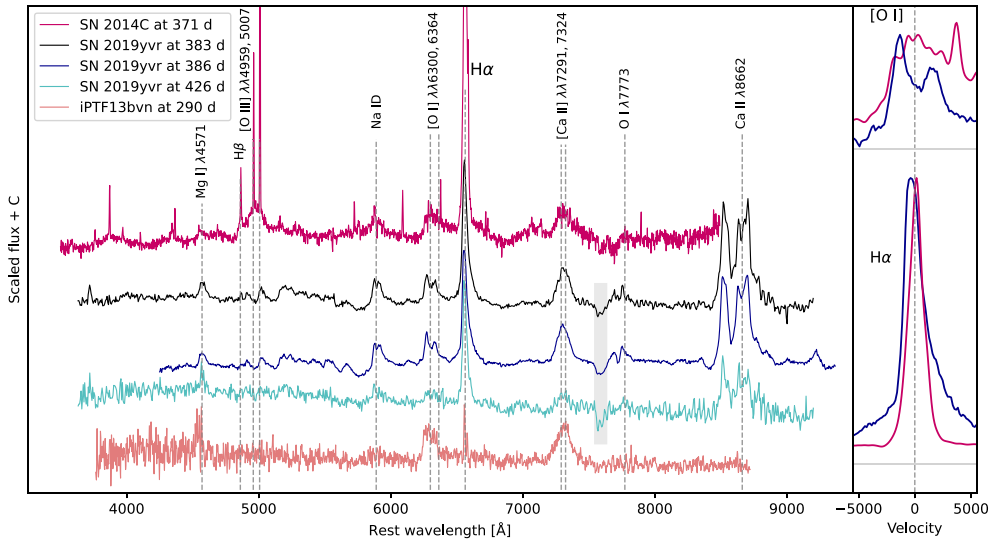

Figure 4. Left panel: nebular spectra of SN 2019yvr compared to the transitional object SN 2014C (Milisavljevic et al. 2015), and to its best match in the early phase, iPTF13bvn (Kuncarayakti et al. 2015). Spectra are corrected by redshift and not corrected by extinction. Prominent emission features are identified and labelled. The telluric *A*-band in SN 2019yvr is marked with a shadowed region. Right panel: H α and oxygen doublet profiles of SN 2019yvr (+386 d, blue) and SN 2014C (+ 371 d, pink). The spectrum of SN 2014C has been rebinned in both panels to match the resolution of the SN 2019yvr spectrum. Both interacting events transition to a SN IIn-like spectrum, showing strong H α emission. H α emission lines in iPTF13bvn are not associated with the SN ejecta but with an underlying H II region. Zero velocities are taken at 6300 and 6563 Å.

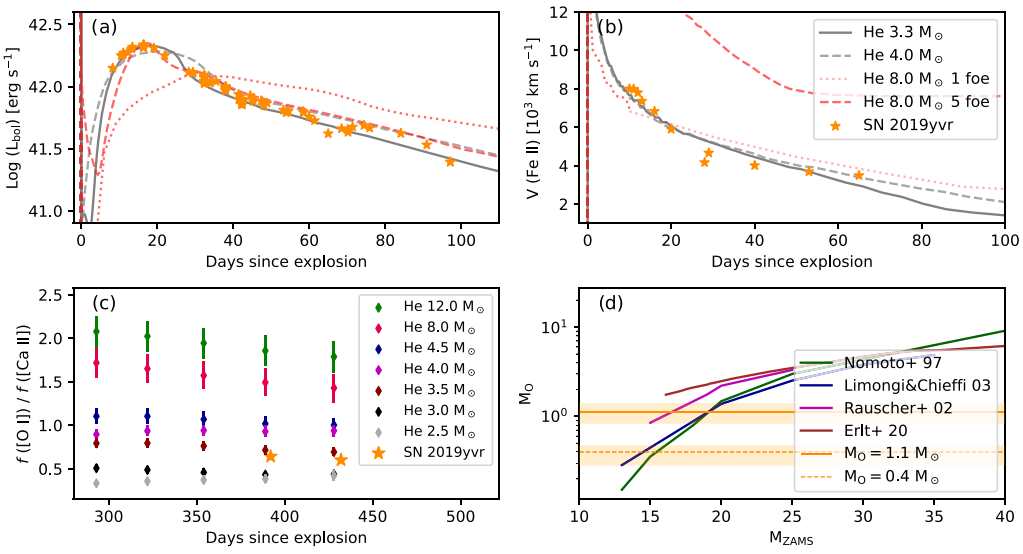

Figure 5. Progenitor mass estimation summary. Panels (a) and (b) show the bolometric light curve and velocity measurements of SN 2019yvr (stars) together with the output of the hydrodynamical models for stars with final He core masses of 3.3, 4.0, and 8.0 $M_\odot$ (solid, dotted, and dashed lines, respectively; see Section 5.1). The preferred model is the least massive. In panel (c), we plot the evolution of oxygen to calcium flux ratio from synthetic spectra (diamonds; Dessart et al. 2023a) and our measurements for SN 2019yvr (stars), which fall in the region between 3.0 and 3.5 $M_\odot$ He core masses (see Section 5.2). Panel (d) shows oxygen yields from Nomoto et al. (1997), Limongi & Chieffi (2003), and Rauscher et al. (2002) for different zero-age main sequence masses and the oxygen core mass derived from [O I] doublet flux (see Section 5.3).

for the flux, as the line profile is not well fitted by one Gaussian only (see Fig. 4; right panel).

We use the grid of models published in Dessart et al. (2023a), where the spectral evolution between 100 and 400 d is calculated for a wide range of initial He masses. We measured the flux ratio [O I]/[Ca II] on these models by fitting a single Gaussian profile centred at 6300 Å for [O I] and at 7304 Å for [Ca II], since the doublets are blended. We compared these results to our measurements in SN 2019yvr at both epochs, as in Fig. 5 panel (c). This approach yields a progenitor with a helium mass between 3.0–3.5 $M_\odot$, which is in agreement with the result from the hydrodynamical model. We note, however, that the line fluxes in the model spectra – which are computed without CSI – are substantially smaller than those obtained for SN 2019yvr. This difference can be due to a contribution from

the CSI in the line fluxes. We cannot ascertain how this may affect the flux ratios. Therefore, this caveat should be kept in mind.

5.3 [O I] doublet flux

Following the procedure described in Jerkstrand et al. (2014), we estimate the oxygen core minimum mass responsible for [O I] doublet flux emission. As in Section 5.2, we assume that the flux comes only from the ejecta and has no contribution from the CSI. This is a strong assumption, since it has been shown that at late times the material excited by CSI can play a major role in the spectral features (Dessart et al. 2023b). Furthermore, the models by Dessart et al. 2023a without CSI have much lower lines fluxes, as do the spectra of the SNe that do not appear to have CSI (SN 2011dh and iPFT13bvn). We thus consider this an upper limit for the pre-SN progenitor mass, and leave further analysis on how the CSI may affect the spectral features for the accompanying paper.

The flux measurement is performed as detailed in Section 4 in the dereddened spectrum at +383 d, due to its high quality and minimal host contamination. Temperature estimation from [O I] λ5577 is not available due to the absence of the line. We therefore assume a typical temperature for these regions of 3000 K. In these conditions, the estimated core oxygen mass is $\sim 1.1 \pm 0.3\,M_{\odot}$. If we assume a higher temperature of 3500 K, the oxygen mass drops to $\sim 0.4 \pm 0.09\,M_{\odot}$.

In both cases, following oxygen production yields from Nomoto et al. (1997), Rauscher et al. (2002), and Limongi & Chieffi (2003), the estimates indicate a progenitor mass between 15 and 20 $M_{\odot}$ [see Fig. 5; panel (d)]. This value is somewhat higher than those obtained in Sections 5.1 and 5.2.

6 CONCLUSIONS

We have presented light curves and spectra of SN 2019yvr that show clear signatures of late-time interaction with a CSM. Time-series observations allowed us to constrain the onset of light curve flattening and H α emission line. We estimated the timing of the CSI and thus the CSM distance to the progenitor, as ~ 6.5–9.1×10^{15} cm in case it is detached from the SN progenitor star. Assuming a steady 50–100 km s^{-1} wind velocity, this implies a mass-loss rate of ~ 3–$7 \times 10^{-5}\,M_{\odot}\,yr^{-1}$, occurring up until ∼20–60 yr prior to the explosion.

Our analysis on the progenitor mass presented in Section 5 is in contradiction with progenitors with pre-SN masses of $\geq 8\,M_{\odot}$. Such a star may have started as a single massive star on the ZAMS and lost the outer layers via vigorous winds, but in the case of SN 2019yvr a less-massive star that lost its H-rich envelope through binary interactions (e.g. Fang et al. 2019; Drout et al. 2023) is a more plausible scenario. It is also possible that the progenitor star experienced a hybrid mass-loss mechanism as that discussed by Fang et al. (2019) and Sun, Maund & Crowther (2023).

The main question lies in how a progenitor with no hydrogen, as indicated by the early spectra, can lead to a H-rich SN at later times. Kilpatrick et al. (2021) suggested two progenitor scenarios for SN 2019yvr: a massive star that went through a series of eruptions in a luminous blue variable (LBV) phase, or a binary system that led to mass-loss episodes timed years to decades ahead of core collapse. Sun et al. (2022) suggested a hot and compact progenitor in a binary system with a cool and inflated YHG companion. Compared with these works, our results are compatible with the binary progenitor scenario and do not favour a single star going through an LBV phase. By studying the host stellar cluster of SN 2014C, Sun, Maund & Crowther (2020) suggested that the progenitor could have been an 11 $M_{\odot}$ star depleted by binary interaction. Otherwise, a single star should have retained its hydrogen-rich envelope to be consistent with the clusters' inferred age. If this is correct, both SNe must have gone through similar evolutionary and mass-loss paths, resulting in stripped progenitors with initial masses well below 20 $M_{\odot}$.

ACKNOWLEDGEMENTS

The Finnish National Agency for Education (EDUFI) supported this research project through an EDUFI Fellowship. HK was funded by the Research Council of Finland projects 324504, 328898, and 353019. MDS is funded by the Independent Research Fund Denmark (IRFD) via Project 2 grant 10.46540/2032-00022B. KM acknowledges support from the Japan Society for the Promotion of Science (JSPS) KAKENHI grant (JP20H00174) and by the JSPS Open Partnership Bilateral Joint Research Project between Japan and Finland (JPJSBP120229923). NUTS is funded in part by the Instrument center for Danish Astrophysics (IDA). LCOGT network data were obtained through OPTICON (PI Stritzinger, programme ID 2020A/031) and NOAO (PI Bose, programme ID NOAO2020A-017) time allocations. Based on observations made with the Nordic Optical Telescope, owned in collaboration by the University of Turku and Aarhus University, and operated jointly by Aarhus University, the University of Turku and the University of Oslo, representing Denmark, Finland and Norway, the University of Iceland and Stockholm University at the Observatorio del Roque de los Muchachos, La Palma, Spain, of the Instituto de Astrofisica de Canarias. Data were also obtained with ALFOSC, which is provided by the Instituto de Astrofisica de Andalucia (IAA) under a joint agreement with the University of Copenhagen and NOT. This work includes data collected at ESO via programme IDs 1103.D-0328, 0105.D-0511, and 1106.D-0811. We thank the Subaru staff for the data taken by the Subaru Telescope (S19B-054); the authors acknowledge the very significant cultural role and reverence that the summit of Maunakea has always had within the indigenous Hawaiian community. We are most fortunate to have the opportunity to conduct observations from this mountain. YZC is supported by the National Natural Science Foundation of China (NSFC,; grant no. 12303054) and the International Centre of Supernovae, Yunnan Key Laboratory (no. 202302AN360001). AP is supported by the PRIN-INAF 2022 project 'Shedding light on the nature of gap transients: from the observations to the models'. LG acknowledges financial support from the Spanish Ministerio de Ciencia e Innovación (MCIN), the Agencia Estatal de Investigación (AEI) 10.13039/501100011033, and the European Social Fund (ESF) 'Investing in your future' under the 2019 Ramón y Cajal programme RYC2019-027683-I and the PID2020-115253GA-I00 HOSTFLOWS project, from Centro Superior de Investigaciones Científicas (CSIC) under the PIE project 20215AT016, and the programme Unidad de Excelencia María de Maeztu CEX2020-001058-M. CPG acknowledges financial support from the Secretary of Universities and Research (Government of Catalonia) and by the Horizon 2020 Research and Innovation Programme of the European Union under the Marie Skłodowska-Curie and the Beatriu de Pinós 2021 BP 00168 programme, from the Spanish Ministerio de Ciencia e Innovación (MCIN) and the Agencia Estatal de Investigación (AEI) 10.13039/501100011033 under the PID2020-115253GA-I00 HOSTFLOWS project, and the programme Unidad de Excelencia María de Maeztu CEX2020-001058-M. TEMB acknowledges financial support from the Spanish Ministerio de Ciencia e Innovación (MCIN), the Agencia Estatal de Investigación (AEI) 10.13039/501100011033, and the European Union Next Generation EU/PRTR funds under the 2021 Juan de la

Cierva programme FJC2021-047124-I and the PID2020-115253GA-I00 HOSTFLOWS project, from Centro Superior de Investigaciones Científicas (CSIC) under the PIE project 20215AT016, and the programme Unidad de Excelencia María de Maeztu CEX2020-001058-M. SM acknowledges support from the Research Council of Finland project 350458. MN is supported by the European Research Council (ERC) under the European Union's Horizon 2020 research and innovation programme (grant agreement no. 948381) and by UK Space Agency grant no. ST/Y000692/1. GP acknowledges support from ANID through Millennium Science Initiative Programs ICN12_009.

DATA AVAILABILITY

Nebular spectra are available in the Wiserep (Yaron & Gal-Yam 2012) database (https://www.wiserep.org/).

REFERENCES

Appenzeller I. et al., 1998, The Messenger, 94, 1
Bersten M. C., Benvenuto O., Hamuy M., 2011, ApJ, 729, 61
Buzzoni B. et al., 1984, The Messenger, 38, 9
Chandra P., Chevalier R. A., Chugai N., Milisavljevic D., Fransson C., 2020, ApJ, 902, 55
Chevalier R. A., Fransson C., 1994, ApJ, 420, 268
Chugai N. N., Chevalier R. A., 2006, ApJ, 641, 1051
Dessart L., Hillier D. J., Sukhbold T., Woosley S. E., Janka H. T., 2021, A&A, 656, A61
Dessart L., Hillier D. J., Woosley S. E., Kuncarayakti H., 2023a, A&A, 677, A7
Dessart L., Gutiérrez C. P., Kuncarayakti H., Fox O. D., Filippenko A. V., 2023b, A&A, 675, A33
Dimitriadis G., 2019, Transient Name Server Classification Report, No. 2019-2736
Dimitriadis G., Foley R. J., Siebert M. R., Kilpatrick C. D., Corbett H. T., 2019, Astron. Telegram, 13375, 1
Drout M. R., Götberg Y., Ludwig B. A., Groh J. H., de Mink S. E., O'Grady A. J. G., Smith N., 2023, preprint (arXiv:2307.00061)
Ergon M. et al., 2015, A&A, 580, A142
Fang Q., Maeda K., Kuncarayakti H., Sun F., Gal-Yam A., 2019, Nat. Astron., 3, 434
Fang Q. et al., 2022, ApJ, 928, 151
Filippenko A. V., Matheson T., Barth A. J., 1994, AJ, 108, 2220
Fransson C., Chevalier R. A., 1989, ApJ, 343, 323
Fransson C. et al., 2002, ApJ, 572, 350
Fremling C. et al., 2016, A&A, 593, A68
Jerkstrand A., Smartt S. J., Fraser M., Fransson C., Sollerman J., Taddia F., Kotak R., 2014, MNRAS, 439, 3694
Jerkstrand A., Ergon M., Smartt S. J., Fransson C., Sollerman J., Taubenberger S., Bersten M., Spyromilio J., 2015, A&A, 573, A12
Kilpatrick C. D. et al., 2021, MNRAS, 504, 2073
Kuncarayakti H. et al., 2015, A&A, 579, A95
Kuncarayakti H. et al., 2018, ApJ, 854, L14
Kuncarayakti H. et al., 2022, ApJ, 941, L32
Limongi M., Chieffi A., 2003, ApJ, 592, 404
Liu Y.-Q., Modjaz M., Bianco F. B., Graur O., 2016, ApJ, 827, 90
Lyman J. D., Bersier D., James P. A., 2014, MNRAS, 437, 3848
Maeda K. et al., 2007, ApJ, 658, L5
Maeda K. et al., 2015, ApJ, 807, 35
Margutti R. et al., 2017, ApJ, 835, 140
Masci F. J. et al., 2019, PASP, 131, 018003
Matheson T., Filippenko A. V., Ho L. C., Barth A. J., Leonard D. C., 2000, AJ, 120, 1499
Mauerhan J. C., Filippenko A. V., Zheng W., Brink T. G., Graham M. L., Shivvers I., Clubb K. I., 2018, MNRAS, 478, 5050
Milisavljevic D. et al., 2015, ApJ, 815, 120
Muller T., Antilen J., Wiseman P., Yaron O., 2019, Transient Name Server Classification Report, No. 2019-2903
Noguchi K. et al., 2002, PASJ, 54, 855
Nomoto K., Hashimoto M., 1988, Phys. Rep., 163, 13
Nomoto K., Hashimoto M., Tsujimoto T., Thielemann F. K., Kishimoto N., Kubo Y., Nakasato N., 1997, Nucl. Phys. A, 616, 79
Patat F., Chugai N., Mazzali P. A., 1995, A&A, 299, 715
Podsiadlowski P., Langer N., Poelarends A. J. T., Rappaport S., Heger A., Pfahl E., 2004, ApJ, 612, 1044
Rauscher T., Heger A., Hoffman R. D., Woosley S. E., 2002, ApJ, 576, 323
Rodríguez Ó., Maoz D., Nakar E., 2022, ApJ, 955, 71
Schlafly E. F., Finkbeiner D. P., 2011, ApJ, 737, 103
Schlegel E. M., 1990, MNRAS, 244, 269
Shappee B. J. et al., 2016, ApJ, 826, 144
Smartt S. J. et al., 2015, A&A, 579, A40
Smith N., 2014, ARA&A, 52, 487
Srivastav S., Anupama G. C., Sahu D. K., 2014, MNRAS, 445, 1932
Stritzinger M. et al., 2012, ApJ, 756, 173
Stritzinger M. D. et al., 2018, A&A, 609, A135
Stritzinger M. D. et al., 2023a, preprint (arXiv:2309.05031)
Stritzinger M. D. et al., 2023b, A&A, 675, A82
Sun N.-C., Maund J. R., Crowther P. A., 2020, MNRAS, 497, 5118
Sun N.-C., Maund J. R., Crowther P. A., Hirai R., Kashapov A., Liu J.-F., Liu L.-D., Zapartas E., 2022, MNRAS, 510, 3701
Sun N.-C., Maund J. R., Crowther P. A., 2023, MNRAS, 521, 2860
Taddia F. et al., 2013, A&A, 555, A10
Tartaglia L. et al., 2021, A&A, 650, A174
Thomas B. P. et al., 2022, ApJ, 930, 57
Tonry J. et al., 2019, Transient Name Server Discovery Report, No. 2019-2726
Vinko J. et al., 2017, ApJ, 837, 62
Woosley S. E., Langer N., Weaver T. A., 1993, ApJ, 411, 823
Yaron O., Gal-Yam A., 2012, PASP, 124, 668
Yoon S.-C., 2017, MNRAS, 470, 3970

SUPPORTING INFORMATION

Supplementary data are available at *MNRASL* online.

suppl_data

Please note: Oxford University Press is not responsible for the content or functionality of any supporting materials supplied by the authors. Any queries (other than missing material) should be directed to the corresponding author for the article.

[1]*Instituto de Astrofísica de La Plata, CONICET, B1900FWA, La Plata, Argentina*
[2]*Facultad de Ciencias Astronómicas y Geofísicas Universidad Nacional de La Plata, Paseo del Bosque S/N B1900FWA, La Plata, Argentina*
[3]*Kavli Institute for the Physics and Mathematics of the Universe (WPI), The University of Tokyo, Kashiwa, 277-8583 Chiba, Japan*
[4]*Department of Physics and Astronomy, University of Turku, FI-20014 Turku, Finland*
[5]*Finnish Centre for Astronomy with ESO (FINCA), University of Turku, FI-20014, Finland*
[6]*Department of Physics and Astronomy, Aarhus University, Ny Munkegade 120, DK-8000 Aarhus C, Denmark*
[7]*Department of Astronomy, Kyoto University, Kitashirakawa-Oiwake-cho, Sakyo-ku, Kyoto 606-8502, Japan*
[8]*Interdisciplinary Theoretical and Mathematical Sciences Program (iTHEMS), RIKEN, Wako, Saitama 351-0198, Japan*
[9]*Department of Physics, University of California, Berkeley, CA 94720, United States of America*
[10]*Institut d'Astrophysique de Paris, CNRS-Sorbonne Université, 98 bis boulevard Arago, F-75014 Paris, France*

[11]*The Oskar Klein Centre, Department of Astronomy, Stockholm University, AlbaNova, SE-10691 Stockholm, Sweden*
[12]*Max-Planck-Institut für Astrophysik, Karl-Schwarzschild-Str. 1, D-85748 Garching, Germany*
[13]*Astrophysics Research Institute, Liverpool John Moores University, 146 Brownlow Hill, Liverpool L3 5RF, UK*
[14]*Metsähovi Radio Observatory, Aalto University , Metsähovintie 114, FI-02540 Kylmälä, Finland*
[15]*Department of Electronics and Nanoengineering, Aalto University , P.O. BOX 15500, FI-00076 AALTO, Finland*
[16]*Department of Physics, Virginia Tech, Blacksburg, VA 24061, USA*
[17]*Department of Astronomy, The Ohio State University, 140 W. 18th Avenue, Columbus, OH 43210, USA*
[18]*Yunnan Observatories, Chinese Academy of Sciences, Kunming 650216, P.R. China*
[19]*Key Laboratory for the Structure and Evolution of Celestial Objects, Chinese Academy of Sciences, Kunming 650216, P.R. China*
[20]*International Centre of Supernovae, Yunnan Key Laboratory, Kunming 650216, P.R. China*
[21]*INAF - Osservatorio Astronomico di Padova, Vicolo dell'Osservatorio 5, I-35122 Padova, Italy*
[22]*INAF - Osservatorio Astronomico di Brera, Via E. Bianchi 46, I-23807 Merate (LC), Italy*
[23]*European Southern Observatory, Alonso de Córdova 3107, Casilla 19, Santiago, Chile*
[24]*Graduate Institute of Astronomy, National Central University, 300 Jhongda Road, 32001 Jhongli, Taiwan*
[25]*Institute of Space Sciences (ICE-CSIC), Campus UAB, Carrer de Can Magrans, s/n, E-08193 Barcelona, Spain*
[26]*Institut d'Estudis Espacials de Catalunya (IEEC), E-08034 Barcelona, Spain*
[27]*Astronomical Observatory, University of Warsaw, Al. Ujazdowskie 4, PL-00-478 Warszawa, Poland*
[28]*School of Physics and Astronomy, Cardiff University, Queens Buildings, The Parade, Cardiff CF24 3AA, UK*
[29]*School of Sciences, European University Cyprus, Diogenes Street, Engomi, 1516, Nicosia, Cyprus*
[30]*Astrophysics Research Centre, School of Mathematics and Physics, Queens University Belfast, Belfast BT7 1NN, UK*
[31]*Instituto de Alta Investigación, Universidad de Tarapacá, Casilla 7D, 1001236, Arica, Chile*
[32]*Astrophysics Research Centre, School of Mathematics and Physics, Queen's University Belfast, Belfast BT7 1NN, UK*

This paper has been typeset from a TEX/LATEX file prepared by the author.